

Stokes Diagnostis of 2D MHD-simulated Solar Magnetogranulation

V.A. Sheminova

© Springer ●●●●

Abstract

We study the properties of solar magnetic fields on scales less than the spatial resolution of solar telescopes. A synthetic infrared spectropolarimetric diagnostics based on a 2D MHD simulation of magnetoconvection is used for this. We analyze two time sequences of snapshots that likely represent two regions of the network fields with their immediate surrounding on the solar surface with the unsigned magnetic flux density of 300 G and 140 G. In the first region we find from probability density functions of the magnetic field strength that the most probable field strength at $\log \tau_5 = 0$ is equal to 250 G. Weak fields ($B < 500$ G) occupy about 70% of the surface, while stronger fields ($B > 1000$ G) occupy only 9.7% of the surface. The magnetic flux is -28 G and its imbalance is -0.04 . In the second region, these parameters are correspondingly equal to 150 G, 93.3%, 0.3%, -40 G, and -0.10 . We estimate the distribution of line-of-sight velocities on the surface of $\log \tau_5 = -1$. The mean velocity is equal to 0.4 km s^{-1} in the first simulated region. The averaged velocity in the granules is -1.2 km s^{-1} and in the intergranules is 2.5 km s^{-1} . In the second region, the corresponding values of the mean velocities are equal to 0, -1.8 , 1.5 km s^{-1} . In addition we analyze the asymmetry of synthetic Stokes-V profiles of the Fe I 1564.8 nm line. The mean values of the amplitude and area asymmetry do not exceed 1%. The spatially smoothed amplitude asymmetry is increased to 10% while the area asymmetry is only slightly varied.

Keywords: Magnetic fields, Photosphere; Velocity Fields, Photosphere; Granulation; Spectral Line, Intensity and Diagnostics

1. Introduction

Despite a long history of the solar magnetic field studies and enormous number of publications, many problems remain unsolved. One of these problems concerns solar small-scale magnetic fields in the photosphere outside sunspots.

Main Astronomical Observatory, National Academy of Sciences of Ukraine, 27 Akademika Zabolotnoho St., Kyiv, 03680 Ukraine email: shem@mao.kiev.ua

The determination of the fine structure of magnetic elements is difficult because of their very weak magnetic flux and insufficient resolution. Present-day spectropolarimetric observations of absorption lines which provide basic information about the magnetic field structure have a spatial resolution not better than a few tenths of arcsec. To resolve separate small magnetic features in the photosphere and to obtain information about their properties and structure, we need a resolution better than $0''.1$. It is found that the small-scale magnetic elements should be smaller than 50-100 km (Domínguez Cerdeña, Sánchez Almeida, Kneer, 2003; Khomenko *et al.*, 2003). Furthermore, Cameron, Galloway (2005) have shown that any magnetic element should be structured down to the turbulent magnetic diffusivity length-scales of 10 km. Such small structures cannot be resolved with the present-day telescopes. But it is possible to improve our understanding of the nature of solar small-scale fields with the use of the self-consistent models of solar photosphere regions. These models are constructed on the basis of realistic physics with the use of the equations of radiation magnetohydrodynamics (MHD). Such time-dependent MHD models allow us to study in detail the evolution, dynamics, and structure of magnetic elements. The spatial resolution of the numerical simulation is a few grid points corresponding to a few tens of kilometers (Sánchez Almeida, 2006).

A detailed review of realistic MHD simulations of solar magnetoconvection can be found in Schüssler (2003) and Steiner (2007). Three-dimensional (3D) models of the solar magnetoconvection were first considered in the pioneering work of Nordlund (1985). Later Cattaneo (1999) has studied the local dynamo mechanism using idealized 3D simulation of thermal magnetoconvection in the Boussinesq approximation in the quiet photosphere. Realistic 3D MHD models were further developed in Stein, Nordlund, (2000, 2006); Carlsson *et al.* (2004); Vögler *et al.* (2005); Steiner *et al.* (2008). The 3D MHD simulation are complemented by two-dimensional (2D) MHD simulation (*e.g.*, Deinzer *et al.*, 1984; Brandt, Gadun, 1995; Atroshchenko, Sheminova, 1996a, 1996b; Grossmann-Doerth, Schüssler, Steiner, 1998; Gadun, 2000). The analysis of 2D simulations of convection (Gadun, Solanki, Johannesson, 1999; Ploner, Solanki, Gadun, 1999) showed that 2D models reproduce many features of 3D convection, although cannot represent realistic flow patterns (Asplund *et al.*, 2000). However, 2D MHD models quite adequately reproduce small-scale phenomena and are useful in studying the properties of magnetic elements (*e.g.*, Grossmann-Doerth, Schüssler, Steiner, 1998; Gadun, Sheminova, Solanki, 1999a).

The 2D MHD models by Gadun, Sheminova, Solanki (1999a) first presented the evolution of magnetogranulation of mixed-polarity solar regions over 2 hours of solar time. Based on these models Sheminova, Gadun (2000) have considered formation and destruction of fluxtubes and have obtained the observable signatures of convective collapse in Stokes-V profiles. These signatures were confirmed by spectropolarimetric observations of Bellot Rubio *et al.* (2001) and Nagata *et al.* (2008). A clear relation was found between field strength and magnetic inclination (Gadun *et al.*, 2001). This result is in qualitative agreement with observations (Lites, Skumanich, Martínez Pillet, 1998). It was found that the predominantly horizontal weak fields are located in the photospheric layers of granules (Gadun, 2000). This fact was confirmed by new Hinode observations

(Lites *et al.*, 2008). An example of flux recycling events in this simulation was discovered by Ploner *et al.* (2001a). Later, 3D MHD simulation by Stein, Nordlund (2002) confirmed that a local short-period recirculation can arise near the surface under the conditions of strong stratification and asymmetric convective flows. This mechanism can provide a high rate of flux emergence through the solar surface.

The 2D MHD models (Gadun, Sheminova, Solanki, 1999a) were also used in the Stokes diagnostics of small-scale magnetic fields (Sheminova, 1999, 2003, 2004, 2005; Sheminova, Gadun, 2000; Ploner *et al.*, 2001b). In this paper a Stokes diagnostics of simulated 2D magnetogranulation with two different magnetic flux densities is presented.

As to the terminology, the term "magnetogranulation" means granulation in the presence of magnetic field. The compact magnetic elements are similar to sheet-like structures extending along the lanes ("fluxsheets") in the 2D Cartesian description. We use for them the traditional definition "fluxtubes". To avoid confusion in defining the magnetic field characteristics we use the following: B is the magnitude of the magnetic vector, i.e., the field strength; $\langle B \rangle$ is the average field strength over given region; B_z is the vertical component of the magnetic vector; $\langle |B_z| \rangle$ is the unsigned (absolute) flux density; $\langle B_z \rangle$ is the flux density. The magnetic flux F is the area integral over the field vector when the line of sight is perpendicular to the area of integration, i.e., it is the longitudinal magnetic flux.

The paper is arranged as follows: Section 2 shortly describes the 2D MHD simulations used in our analysis. The spectral synthesis of Stokes profiles is considered in Section 3. The results of Stokes diagnostics are presented in Section 4, and Section 5 gives our conclusions.

2. Numerical 2D MHD Models of Solar Magnetogranulation

The complete system of radiative magnetohydrodynamical equations is used for the 2D MHD simulation of the upper solar convection zone and the photosphere (Gadun, Sheminova, Solanki, 1999a). We adopt the approximation that the medium is compressible, partially ionized, stratified by gravity, and coupled with the radiation. The simulations start with a 2D hydrodynamical (HD) model of the solar granulation obtained earlier by Gadun, Solanki, Johannesson (1999). The code for the integration of the MHD equations represents an extension of the radiation-hydrodynamic code that is described in detail by Gadun, Solanki, Johannesson (1999). Note that the radiative transfer is treated in the grey approximation. The magnetic field is described by the vector potential, so that the divergence of magnetic field strength is always zero in the simulated region.

In the first simulation the computational domain spans 3920 km horizontally and 1820 km vertically, with the grid step of 35 km corresponding to 112×52 grid-points. The atmosphere is extended from 1135 km below to 685 km above the geometrical height $h = 0$ or $\tau_R = 1$, τ_R being the Rosseland optical depth (Figure 1a). This simulation ran for 2 hours of the solar time.

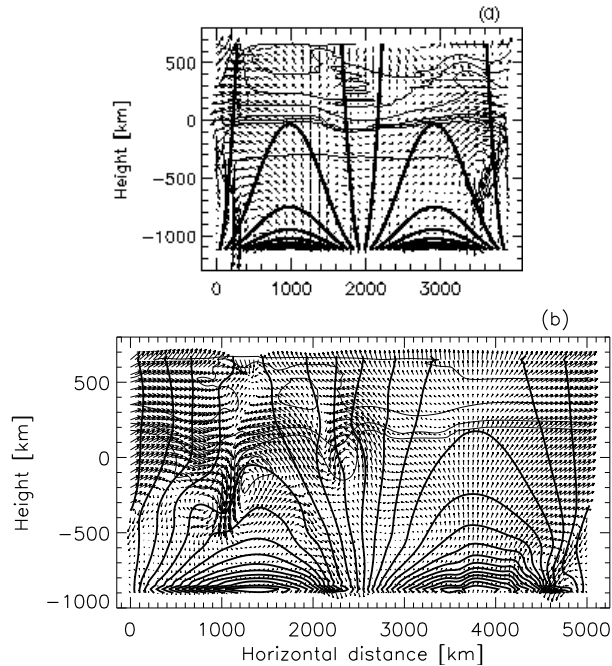


Figure 1. (a): snapshot of the initial HD model and the initial configuration of magnetic field in the first MHD simulation with the spatially averaged magnetic field strength $\langle B \rangle = 54$ G. (b): the same but for $t = 30$ s in the second MHD simulation with $\langle B \rangle = 1.6$ G. Thick curves: magnetic field lines. Thin curves: isotherms from top to bottom indicate the temperature of 4000, 5000, 6000, 7000, 8000, 9000, 10000, and 12000 K. Arrows: velocity field.

In the second simulation the grid size of the computational domain is 202×64 grid-points (or 5050×1600 km, Figure 1b). The corresponding grid step is 25 km. The atmosphere covers 900 km below and 700 km above the level $h = 0$. The total simulation time is 4.5 hours.

The side boundaries are periodic while the upper and lower boundaries are open. We adopt $B_x = 0$ and $dB_z/dz = 0$ at the upper and lower boundaries, where B_x is the horizontal component of the magnetic field. The configuration of the initial magnetic field is bipolar (Figure 1). The total initial field flux over the computational box is zero. The mean initial magnetic field strength $\langle B \rangle$ over the entire computational domain in the first and second simulations is 54 and 1.6 G. Processing and amplification of the initial field is resulted in additional magnetic unsigned flux, which is varied with time. The mechanisms of the magnetic field growth were considered by Gadun (2000).

The initial MHD model includes the initial magnetic field superposed on the HD model of solar granulation. A transient of the order of 30 min is needed for the magnetic field to be consistent with the HD structure. In general, the simulation may be arbitrarily divided into three stages. Figure 2 shows the evolution of the brightness, of the vertical velocity, and of the vertical magnetic field in the first simulation at $\tau_R = 1$. The initial period (0–20 min) is determined mainly by the initial conditions: the field lines are forced out by convective

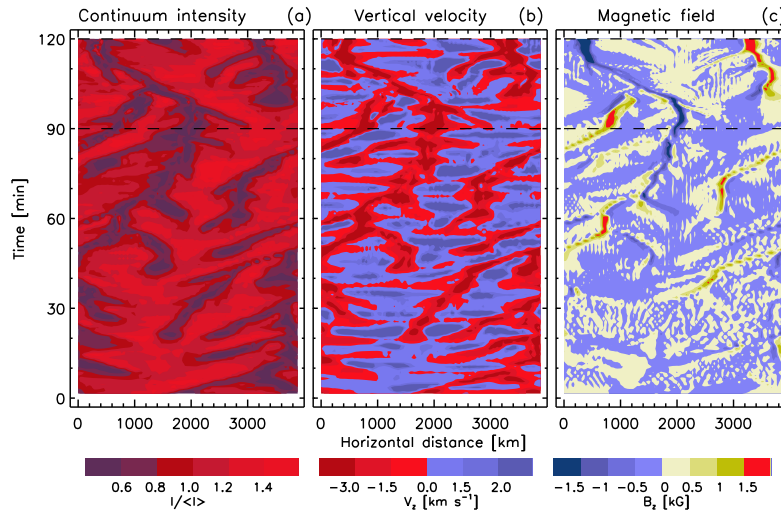


Figure 2. The maps showing the spatial-temporal evolution of the continuum intensity at $\lambda = 500$ nm (a), the vertical component of velocity field (b), and magnetic field (c) at the level $\log \tau_R = 0$ in the first MHD simulation. The horizontal axis indicates position on the Sun, while time increases upwards. Positive values of the velocity shown in blue correspond to upflows while downflows are indicated in red. The different scales for positive and negative values of vertical magnetic component B_z indicate negative and positive polarity field. Dashed lines mark the selected region for Stokes diagnostics with absolute flux density of 300 G (300-MHD).

motions to the region of downflows. The field lines are partially reconnected and the local field concentrations are dissipated. In the period, $t = 20$ – 30 min, no clearly-defined features of the magnetic field is present. This can be seen from the B_z -distribution (Figure 2c). Therefore the magnetic field has a chaotic (turbulent) distribution up to $t = 30$ min. Later on the field becomes structured: it is enhanced in intergranular lanes; new thin flux tubes begin to form at the moment of the granule fragmentation; fields of different polarities are separated; the field in strong flux tubes tends to be vertical, while it is more horizontal above granules. The structural changes of the magnetic field, the brightness field, and the vertical velocity field are similar in appearance. After $t = 50$ min the bright points appear within the intergranular lanes (Figure 2a) corresponding to the regions with compact strong predominantly vertically orientated magnetic field (Figure 2c) and strong downflows (Figure 2b).

The spatial-temporal changes of the magnetogranulation in the first simulation (Figure 2) can be considered as a filtergram, a Dopplergram, and a magnetogram on the solar surface obtained with a slit which cuts 35 km strips at each instant of time every 30 or 60 sec. By analogy with observations we can use a sample of snapshots for Stokes diagnostics. We select the 30 min sample of snapshots in the $t = 90.5$ – 120 min interval marked by dashed lines in Figure 2. It contains 56 snapshots. Four of them are taken at $t = 90.5$ – 93.5 min every 1 min, whereas the timestep of the rest is 30 sec. B_z in this sample varies from -2870 to 2350 G. Several bright points (BPs) are present in this simulated region. The mean unsigned field strength $\langle B \rangle$ at the optical depth $\log \tau_R = 0$ over all these snapshots is 498 G. The mean unsigned longitudinal field strength (or

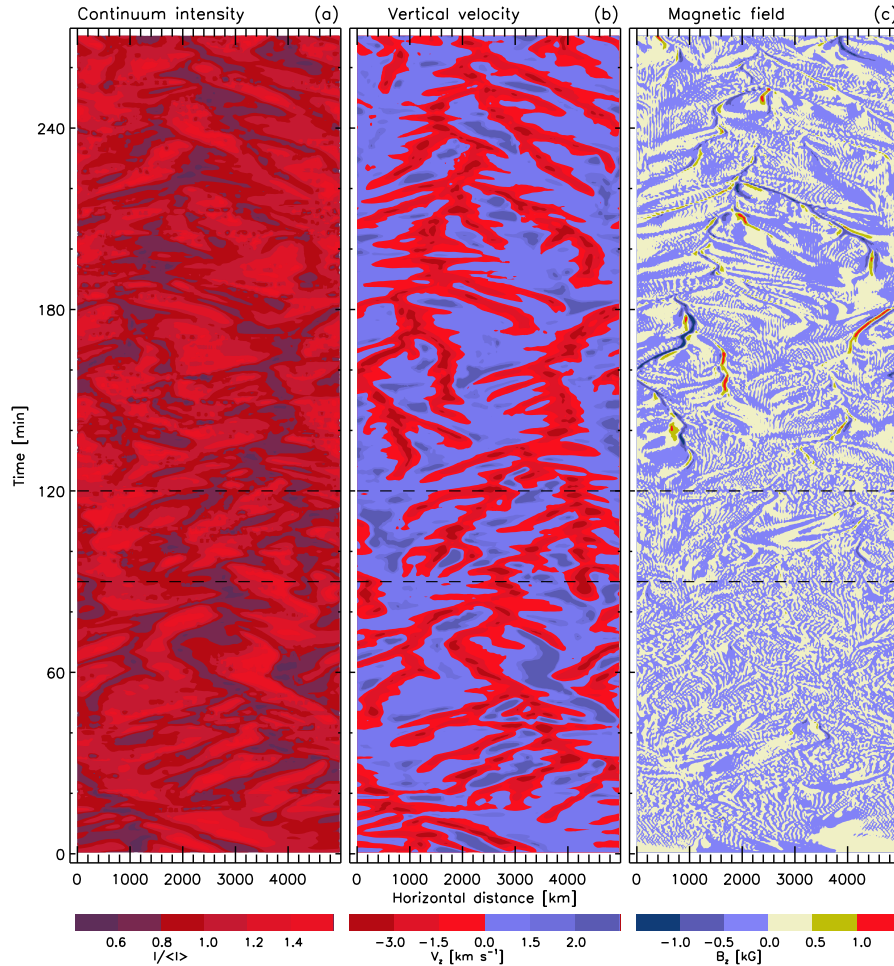


Figure 3. The same as in Figure 2 but for the second MHD simulation. Dashed lines mark the selected region for Stokes diagnostics with absolute flux density of 140 G at $\log \tau_R = 0$ (140-MHD).

absolute flux density) $\langle |B_z| \rangle$ amounts to 300 G at $\log \tau_R = 0$. The large difference between $\langle B \rangle$ and $\langle |B_z| \rangle$ can be explained by the presence of the relatively weak almost horizontally oriented fields which fill the granular surface. The 30 min sample of snapshots with absolute flux density of 300 G will be called hereafter 300-MHD.

The spatial-temporal evolution of the simulated magnetogranulation in the second simulation with the initial $\langle B \rangle = 1.6$ G is shown in Figure 3. The BPs are not seen in the continuum at $\lambda 500$ nm (Figure 3a). Why? According to the simulation only weak-field fluxtubes are formed. It is believed that the BPs are caused by lateral radiation leakage scattering from deeper layers of the magnetic element. The magnetic field of the weak-field fluxtubes is not strong enough for their evacuation in their low photosphere levels. We assume that such

conditions can occur in the solar photosphere too. A detailed study of observed BPs can be found in Sánchez Almeida *et al.* (2004), de Wijn, Rutten, Tarbell (2005), and Berger, Rouppe van der Voort, Löfdahl (2007). These authors find that BPs are common in the quiet Sun. According to observations of G-band BPs (Sánchez Almeida *et al.*, 2004) their density is 0.3 Mm^{-2} while de Wijn, Rutten, Tarbell (2005) found lower density, $0.02\text{--}0.05 \text{ Mm}^{-2}$. In addition, there are many BPs with an intensity smaller than that of the mean photosphere (Sánchez Almeida *et al.*, 2004). The BPs deficiency in our second simulation contradicts the observations in this respect. 60 snapshots are taken from second simulation in the range from 90 to 120 min (marked on Figure 3). B_z is varied from -1070 to 1300 G. The mean unsigned field strength $\langle B \rangle$ for this sample is 252 G at the optical depth $\log \tau_R = 0$. The unsigned magnetic flux density $\langle |B_z| \rangle$ is 140 G. This sample of 60 snapshots called 140-MHD is used later in Stokes diagnostics.

3. Spectral Synthesis

The Fe I λ 1564.8 nm line is the most Zeeman-sensitive spectral line in the solar spectrum because of its largest Stokes-V peak separation. This separation is unhampered by thermal line broadening effects, so that the field strength measurement becomes basically model independent if the magnetic field were constant. Therefore one can directly determine the field strength from V-peak separations without the use of atmospheric models. A limitation of this method is that this line is weakened in kG magnetic concentrations more than other typical lines (Sánchez Almeida, Lites, 2000). To verify a diagnostic potential of this line we compare B derived from V-peak separations of the synthetic profiles and original B taken from the results of simulations. We find satisfactory agreement between them for $B > 200$ G. As to observations, infrared polarimetry allows to measure the V signals which are above the noise level of $0.0002\text{--}0.0003$ in units of continuum intensity I_c (*e.g.*, Khomenko *et al.*, 2003). This precision is sufficient to recover strong fields in observations with high spatial resolution ($0.''5$ and better). Note that Fe I 1564.8 nm line is formed under the LTE conditions and its temperature sensitivity is low (*e.g.*, Solanki, Rüedi, Livingston, 1992). It is often used in polarimetric measurements (*e.g.*, Lin, 1995; Meunier, Solanki, Livingston, 1998; Khomenko *et al.*, 2003) as well as for the analysis of MHD simulation (*e.g.*, Sheminova, 2003; Khomenko *et al.*, 2005a; Shelyag *et al.*, 2007).

For our calculation we use the same line parameters as that in the recent paper by Shelyag *et al.* (2007). We adopt the excitation potential of 5.43 eV, the oscillator strength of $\log(gf) = -0.675$, and the iron abundance of $A_{Fe} = 7.43$. Collisional broadening by neutral atoms is calculated following Barklem, Piskunov, O'Mara (2000). We do not take into account any micro- and macro-turbulent velocities. The line profiles are computed with a spectral resolution of $5 \text{ m}\text{\AA}$ in the wavelength range $\pm 1.5 \text{ \AA}$ around the line center for four Stokes parameters at the solar disc center in every vertical column along the line-of-sight of every snapshot. The solution of the Unno-Rachkovskii equations for the polarized light is obtained by a fifth-order Runge-Kutta-Felberg method. We use our SPANSAT

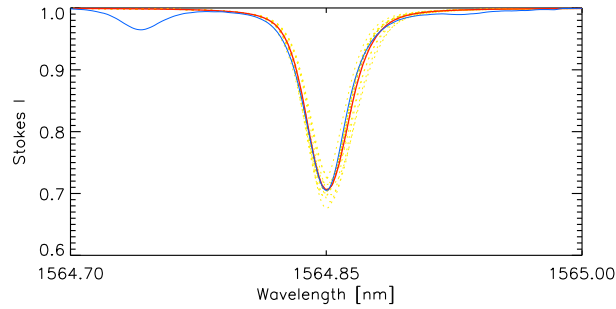


Figure 4. Comparison of the spatially averaged synthetic Fe I 1564.8 nm line profile (shown in red) and the observed quiet-Sun profile (blue) from the spectral atlas of Delbouille, Roland, and Neven (1973). The red profile is the average over the profiles (shown in yellow) calculated from each of 12 snapshots (140-MHD run).

code (Gadun, Sheminova, 1988) modified for the calculation of Stokes profiles. As a result we obtain 6272 Stokes-V profiles from the 300-MHD run and 12 120 from the 140 MHD run. These two samples of synthetic V profiles are used for Stokes diagnostics of simulated regions with different unsigned flux densities.

Note that the observed Stokes-V profiles are strongly affected by noise. Therefore, when deriving the properties of the synthetic line profiles the noise should be considered too. In our special case the minimum of the mean amplitude of synthetic Stokes-V signals is $a_V = 0.0007$ (a maximum is 0.15), while the noise level of Stokes-V observations is lower (0.0002–0.0003, Domínguez Cerdeña, Sánchez Almeida, Kneer, 2006b; 0.0005, Lites, 2002). It follows that we need not to take into account noise in the analysis of the synthetic Stokes-V profiles.

Together with the Stokes profiles we calculate the contribution and response functions described by Grossmann-Doerth, Larsson, Solanki (1988). We find that the effective formation depths of four Stokes profiles differ slightly from each other. Previously they were studied in detail by Sheminova (2003). The mean level of the effective absorption in the photosphere for the Stokes-V peaks of the 1564.8 nm line changes from $\log \tau_5 = -0.4$ to $\log \tau_5 = -1.3$, depending on their formation place. τ_5 is the optical depth at λ 500 nm. In order to show how the simulated line profiles agree with observations, we show in Figure 4 the spatially averaged synthetic Stokes-I profile and the observed spectrum of the quiet Sun (Delbouille, Roland, Neven, 1973). The mean synthetic Stokes-I profile is calculated using 12 snapshots with very weak magnetic fields. The snapshots are taken from the 140-MHD run in 0.5 min in the range from 90 min to 96.5 min. The number of snapshots is optimized to exclude the effect of the 5 min oscillations. The average synthetic and observed profiles agree satisfactorily.

We also reduce the spatial resolution of the computed Stokes profiles to the observed spatial resolution. For this we perform a convolution of the synthetic Stokes profiles with the point-spread function (PSF, Khomenko *et al.*, 2005a). The PSF represents a combination of an Airy function appropriate for the German VTT and a Lorentz function describing the image degradation caused by seeing. The PSF involves a 2-dimensional convolution with the synthetic signals in the plane perpendicular to the LOS. In the case of our 2D MHD simulation we

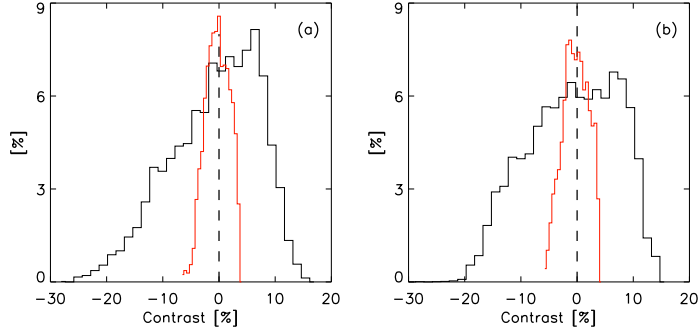


Figure 5. Histograms of continuum intensity contrast at 1564.8 nm. They were obtained for the 300-MHD (a) and 140-MHD (b) regions before (black) and after (red) smearing synthetic continuum intensity with the PSF.

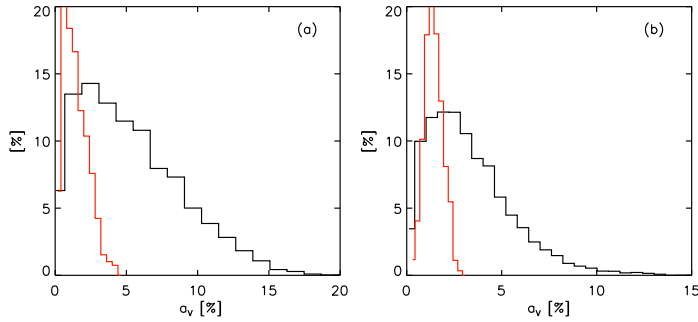


Figure 6. Histograms of mean amplitudes (a_V) derived from the synthetic Stokes-V profiles of the Fe I 1564.8 nm line in the 300-MHD (a) and 140-MHD (b) regions before (black) and after smoothing (red).

have V profiles which change only along one spatial X -coordinate perpendicular to the LOS. We assume that the profiles along the Y -coordinate perpendicular to the LOS is identical to that of X -coordinate. Thus each computed Stokes profile is individually convolved with the PSF to be smeared in the plane perpendicular to the LOS. The free coefficients of the PSF are selected so that the continuum contrast at λ 1564.8 nm after smoothing matches the observed contrast of 3% (Khomenko *et al.*, 2003). Based on this contrast agreement we assume that the resolution of the smoothed images of magnetogranulation is close to the observed resolution of about $1''$ (Khomenko *et al.*, 2003). The synthetic rms contrast is about 8% before and about 3% after smoothing in the two simulated regions. Figure 5 shows the contrast distribution obtained before and after the spatial smoothing of the continuum intensity. Note that the asymmetric shape of the contrast distribution is more pronounced for the simulated region with stronger average magnetic flux.

After smoothing the Stokes-V profiles change substantially. The seeing transforms the majority of the profiles to broader and weaker ones. The amplitudes of red (a_r) and blue (a_b) wings and their mean values, $a_V = (a_r + a_b)/2$, decrease. The relative distribution of a_V is shown in Figure 6. On the average, the amplitudes of the synthetic Stokes-V signals $\langle a_V \rangle = 5.8\%$ (3.6%) before

and 1.7% (1.5%) after smoothing in the 300-MHD (140-MHD) region. They are one order of magnitude larger than the observed $\langle a_V \rangle$ in the internetwork regions (Khomenko *et al.*, 2003; Sánchez Almeida, Domínguez Cerdeña, Kneer, 2003) and are closer to that observed in magnetic network regions. This fact as well as the larger absolute flux density in the simulated regions (by a factor of 10) as compared to the quiet-Sun observations implies that the simulated regions likely correspond to a network regions observed on the solar surface.

The number of Stokes-V profiles with irregular shapes changes considerably after smoothing, specially in the case of 300-MHD. We call the V profiles irregular if they have more than one zero-crossing. The fraction of irregular synthetic profiles for 300-MHD snapshots is 9% before and 58% after spatial smoothing. For 140-MHD snapshots it is 12% and 5%, respectively. The number of irregular Stokes-V profiles increases after smoothing for 300-MHD, but it decreases for 140-MHD. Why do the two simulations behave so differently? Since neighboring V profiles influence each other in the act of smoothing, we considered the shape of many synthetic profiles in detail before and after smoothing. It turns out that magnitude and sign of amplitudes (a_b and a_r) and especially zero-crossing shifts differ dramatically from a profile to a profile in 300-MHD run. The reason is that the range of magnetic field strength and vertical velocities is considerably larger in the 300-MHD region than in the 140-MHD region. Note that according to Domínguez Cerdeña, Sánchez Almeida, Kneer (2006b) 34% of the analyzed observed IR profiles have irregular shape.

The irregular V profiles can introduce additional errors in the evaluation of Stokes-V peak separation, zero-crossing wavelength, area and amplitude asymmetry. Therefore in our analysis only the V profiles with regular shape are used, i.e., with a well-defined zero-crossing.

4. Results of Stokes Diagnostics of Two Simulated Regions

4.1. The Magnetic Field Strength Distribution

How are magnetic fields distributed over the surface of the Sun outside active centers? This question is a hot topic in current research (for reviews, see Steiner, 2003b; Domínguez Cerdeña, Sánchez Almeida, Kneer, 2006a). The weak and strong magnetic fields are strongly mixed in the solar photosphere (*e.g.*, Sánchez Almeida, Lites, 2000; Berger *et al.*, 2004; Rouppe van der Voort *et al.*, 2005). The field lines are very tangled (*e.g.*, Weiss, Proctor, Brownjohn, 2002; Stein, Nordlund, 2006). Many attempts have been made to deduce distribution function of magnetic field on the solar surface. However, there is no agreement between the distribution functions obtained in different papers (*e.g.*, Lin, 1995; Lin, Rimmele, 1999; Sánchez Almeida, Lites, 2000; Collados, 2001; Lites, 2002; Khomenko *et al.*, 2003; Socas-Navarro, Sánchez Almeida, 2002; Domínguez Cerdeña, Sánchez Almeida, Kneer, 2003, 2006a; Martínez González, Collados, Ruiz Cobo, 2006). If the magnetic field distribution on the solar surface is continuous in the range from 0 to 2000 G, the existing discrepancies can be explained by the following reasons: 1) visible and IR lines "see" different structures because of their different magnetic sensitivity (Sánchez Almeida, Lites, 2000; Socas-Navarro, Sánchez

Almeida, 2003; Khomenko *et al.*, 2005b); 2) different techniques use simple or complex atmospheric models (Domínguez Cerdeña, Sánchez Almeida, Kneer, 2006a); 3) spatial resolution of the observed Stokes profiles and cancellation effects are different (Khomenko, Collados, 2007; Orozco Suárez *et al.*, 2007); 4) the noise level in the measurements of very weak Stokes-V signals is varied (Bellot Rubio, Collados, 2003); 5) the difference of the formation depth of different lines used in observations (Martínez González, Collados, Ruiz Cobo, 2006). Besides, the variety of physical processes in different regions leads to different magnetic structures and different magnetic field distributions (Steiner, 2003b).

Realistic simulation of solar magnetoconvection (Atroshchenko, Sheminova, 1996a; Steiner, 1996; Grossmann-Doerth, Schüssler, Steiner, 1998; Stein, Nordlund, 2000; Vögler *et al.*, 2005) has revealed that the magnetic fields in the photosphere are structured from the greatest to the smallest details and have mixed polarities at small scales. There are a few studies in which field strength distributions have been obtained from magnetoconvection simulations (Cattaneo, 1999; Stein, Bercik, Nordlund, 2002; Steiner, 2003a; Vögler *et al.*, 2005; Stein, Nordlund, 2006). We also use the 300-MHD and 140-MHD samples of snapshots from the 2D MHD simulation by Gadun, Sheminova, Solanki (1999a) to determine the magnetic field distribution.

The distribution of field strength on the solar surface is usually characterized by a probability density function, or shortly PDF, (*e.g.*, Domínguez Cerdeña, Sánchez Almeida, Kneer, 2003, 2006a; Steiner, 2003b; Vögler *et al.*, 2005). According to Steiner (2003a) the probability density function $p(B)$ is defined by a probability distribution function,

$$P(B) = \int_0^B p(B)dB,$$

which gives the probability of finding a magnetic field strength less than B at given location within the given field of view. Where $p(B)dB$ is the probability of a magnetic field strength to have at a given location a value in the interval $[B, B + dB]$. The function $p(B)$ is always positive and normalized to unity

$$\int_{-\infty}^{+\infty} p(B) = 1.$$

Its first moment,

$$\langle B \rangle = \int_0^{\infty} Bp(B)dB,$$

gives the mean value of the magnetic field strength. The second moment,

$$\langle B^2 \rangle = \int_0^{\infty} B^2p(B)dB,$$

provides the unsigned magnetic energy density $\langle B^2 \rangle / 8\pi$. In our case $p(B)$ is not continuous because we have a finite number of grid cells, N , with B_i values ($i = 1, \dots, N$). We can obtain a discrete PDF of magnetic field strength

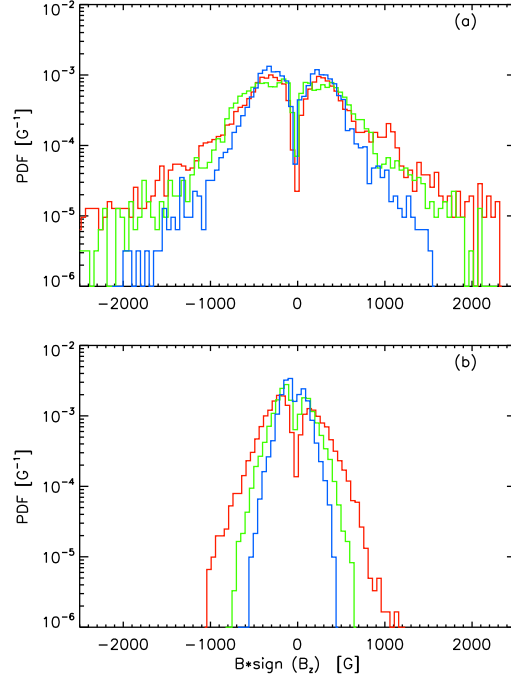


Figure 7. Histograms of probability density function of the signed magnetic field strength in the 300-MHD (a) and the 140-MHD (b) runs at different photospheric levels $\log \tau_5 = 0$ (red), -1 (green), and -2 (blue).

in each simulated region. For this purpose we divide whole range of the field strengths into equal bins of 50 G. Each individual intrinsic field B_i is assigned to one k th bin. The discrete PDF for the k th bin, $[B_k, B_k + \Delta B]$, is defined as $p_k = m_k / (N \Delta B)$, where m_k is the absolute frequency for the k th bin and ΔB is the interval of the bin.

Figure 7 shows histograms of the discrete PDFs of signed magnetic field strengths in the two simulated regions. They show the statistical properties of different layers in the photosphere. The strongest magnetic fields beyond 1 kG are located near $\log \tau_5 = 0$. They decrease with the height in the photosphere.

For comparison we can consider PDFs derived from 3D MHD simulation of magnetoconvection with different initial conditions for magnetic field (Vögler *et al.*, 2005, Fig. 5; Stein, Bercik, Nordlund, 2002, Fig. 5). Vögler *et al.* (2005) used a vertical, homogeneous, unipolar, initial field of 200 G. Stein, Bercik, Nordlund (2002) simulated with no initial magnetic field, but, lately horizontal magnetic fields were advected into the simulated domain by upflows across the lower boundary. Our PDF (Figure 7a) in shape more closely resembles the PDF by Stein, Bercik, Nordlund (2002) than the PDF by Vögler *et al.* (2005) because the initial magnetic field of our simulation and of Stein, Bercik, Nordlund (2002) are similar in appearance. As the simulation of Stein, Bercik, Nordlund (2002) looks the emergence of magnetic flux through solar surface, the same is characteristic of our simulation.

Just as the field strength PDF is derived from Stokes-V observations, we obtain the PDF for simulated region from the synthetic V profiles of the Fe I λ 1564.8 nm line. We use the V peak separations technique to determine B_i in each simulated element of each snapshot. The inferred discrete PDFs of magnetic field strength in the simulated regions are called 15648-PDFs. They are normalized so that their integral is equal to 1 if all N values of B_i of a given sample are considered. If only some portion n of all B_i values is considered, the integral is equal to n/N . Such normalization assumes that remaining portions of the simulated region surface is field-free. It does not change the PDF's shape. Figure 8 (a, b) shows the 15648-PDFs based on the original (violet) and smoothed (blue) Stokes-V profiles in the two simulated regions. The difference between them increases for large field strengths. The original (smoothed) 15648-PDFs derived from the two simulated regions have B_{max} about 330 G (270 G) and about 230 G (250 G), respectively. We can estimate the reliability of the V peak separations technique comparing the PDFs derived from numerical simulation and from synthetic Stokes-V profiles (original and smoothed). It can be seen from Figure 8 (c, d) that the original 15648-PDFs and the MHD-PDFs derived from the simulations at $\log \tau_5 = 0$ are in close agreement in the range of field strengths above 500 G. We conclude that the V-peak separation method is reliable only for $B > 500$ G. The number of fields obtained by this method in the range 0–200 G is zero while it is overestimated in the interval 200–500 G. As a result a maximum of the 15648-PDFs is shifted with respect to a maximum of the MHD-PDFs to stronger fields by 150 G.

Unfortunately, we can not directly compare the 15648-PDFs or the MHD-PDFs with the PDFs of magnetic field strength observed in the network regions. When computing an observed PDF the knowledge of individual filling factors for each analyzed pixel is necessary. Since the filling factors are different for weak and strong fields, taking them into account can dramatically change both the shape of the observed PDF and the magnitude of probability density. For an example one can compare $|B_{app}|$ and true $|B|$ in Figure 3 of Lites (2002). Computation of the filling factors and comparison between PDFs derived by different techniques is not trivial task (Sánchez Almeida, 2004; Domínguez Cerdeña, Sánchez Almeida, Kneer, 2006a). On the other hand, the MHD-PDFs represent the distribution of the field strength of each grid cell of a specific simulated region bounded by the sizes of computation domain.

Let consider the shape of observed PDFs obtained by inversion techniques which derive both true field strengths and their filling factors. Figure 3 in the paper of Lites (2002) presents a histogram of relative occurrence (which is proportional to the probability density function) of absolute true field strength of magnetic network and of their halo. This histogram reveals two peaks around 300–400 G (the halo fields) and 1300–1400 G (the strong network elements). Using the other inversion technique, Socas-Navarro, Sánchez Almeida (2002) found only a one maximum around kG fields in the same network regions that were analyzed by Lites (2002). The MHD-PDFs do not reveal clear bimodal shape. Instead they have one very broad maximum around 200–700 G for the 300-MHD run and 100–400 G for the 140-NHD run. Note the MHD-PDF (300-MHD) in shape is reminiscent of that found in observed quiet regions by Lin

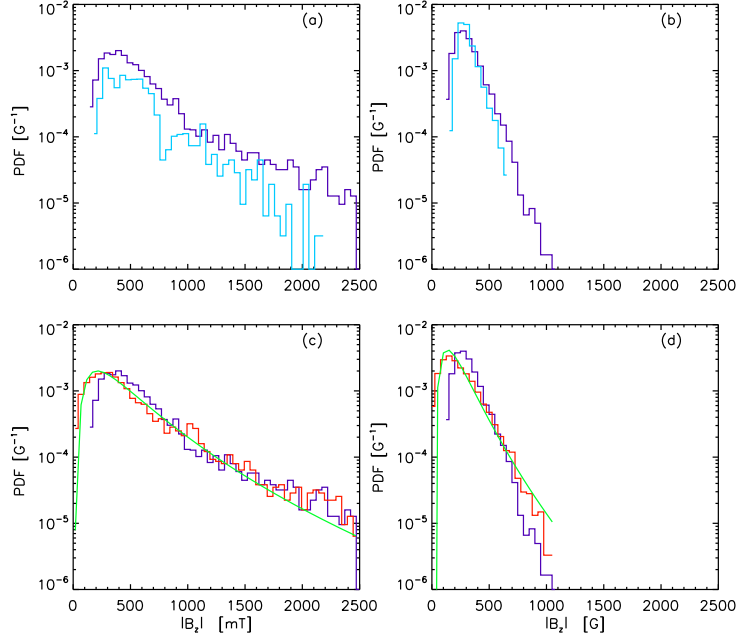


Figure 8. PDFs of the unsigned magnetic field strength in the 300-MHD (a, c) and 140-MHD (b, d) simulated regions: original (violet) and smoothed (blue) 15648-PDFs derived from peak separations of the synthetic Stokes-V profiles of the Fe I 1564.8 nm line without and with spatial smoothing as well as the MHD-PDFs (red) derived from the numerical data at $\log \tau_5 = 0$, and its approximation by the lognormal function (green).

(1995) with a maximum around 300–700 G and Khomenko *et al.* (2003) with a maximum about 350 G. The MHD-PDF (140-MHD) is similar to the PDF derived by Orozco Suárez *et al.* (2007) with a maximum close to 100 G. Note, however, that in this comparison we are ignoring the large fraction of field free photosphere inferred from observations, which is not present in the simulations. Observations show an unsigned flux density one order of magnitude smaller than our simulations.

Figure 7 by Domínguez Cerdeña, Sánchez Almeida, Kneer (2006a) compares the semiempirical reference PDF of the quiet Sun with the PDFs derived from a 3D MHD simulation by Vögler *et al.* (2005). The shape of all these PDFs is different from our MHD-PDFs. The reference PDF for quiet-Sun region has $B_{max} = 13$ G and $\langle |B_z| \rangle = 150$ G. The PDFs derived from three simulations by Vögler *et al.* (2005) with initial field strengths of 10, 50, 200 G have B_{max} about 5, 8, 50 G and $\langle |B_z| \rangle = 25, 100, 270$ G, respectively. Instead, the MHD-PDFs for the 140-MHD, 300-MHD runs have $B_{max} = 150, 250$ G and $\langle |B_z| \rangle = 140, 300$ G. The most probable field strength, B_{max} , in our two simulations is larger than in the internetwork regions in the reference PDF (Domínguez Cerdeña, Sánchez Almeida, Kneer, 2006a) and the simulations by (Vögler *et al.*, 2005). The unsigned flux in the 140-MHD and 300-MHD is closer to the unsigned flux in the 200 G simulation of plages by Vögler *et al.* (2005). On the other hand, our two simulations of magnetogranulation show magnetic

features on the surface level that are similar to elongated sheet-like structures observed along intergranular lanes. They resemble the solar magnetic network. Therefore it is not surprising that the number of weak fields ($B < 100$ G) in our MHD-PDFs is less than in the semiempirical reference PDF by Domínguez Cerdeña, Sánchez Almeida, Kneer (2006a) obtained for the internetwork fields of the quiet Sun.

Following Domínguez Cerdeña, Sánchez Almeida, Kneer (2006a), we calculate the fraction of simulated surface with $B > B^*$,

$$\alpha(B > B^*) = \int_{B^*}^{\infty} p(B)dB,$$

the fraction of unsigned magnetic field strength,

$$\phi(B > B^*) = \frac{1}{\langle B \rangle} \int_{B^*}^{\infty} Bp(B)dB,$$

and the fraction of energy

$$\epsilon(B > B^*) = \frac{1}{\langle B^2 \rangle} \int_{B^*}^{\infty} B^2p(B)dB.$$

We find that about 83% of the surface area in the simulated strong (weak) network is filled by the magnetic fields of 100–1000 G (100–500 G). The fields with $B > 1000$ G occupy 9.7% (0.3%) of the surface area and contribute with 55.2% (0.6%) of the magnetic energy. The fields with $B > 1500$ G have filling factors $\alpha = 4.2\%$ (0) and contribute 32% (0) of the magnetic energy. The weakest fields ($B < 100$ G) occupy a fraction $\alpha = 8\%$ (17%) of the surface area of the simulated region and contribute to the absolute magnetic energy with 0.2% (1.2%).

In agreement with Domínguez Cerdeña, Sánchez Almeida, Kneer (2006a), we also find that the MHD-PDFs of unsigned field strength in the simulated strong (weak) network at the level $\log \tau_5 = 0$ can be satisfactorily approximated by a lognormal distribution

$$p(B) = \frac{1}{\sqrt{\pi}\sigma B} \exp(-(\ln(B/B_0))^2/\sigma^2)$$

with $\sigma = 1.0$ (0.8), and $B_0 = 356$ G (190 G). Figure 8 (c, d, green lines) shows $p(B)$ together with the MHD-PDFs. For comparison, the $p(B)$ derived from the 3D MHD simulation by Vögler *et al.* (2005) with an initial vertical field of 50 G is characterized by $\sigma = 1.7$, $B_0 = 38$ G. These values have been taken by us from Domínguez Cerdeña, Sánchez Almeida, Kneer (2006a). They differ from our values because of the different flux density of magnetic field in the computational domain as well as different initial conditions of the simulation.

4.2. Magnetic Flux and Imbalance

We estimate the magnetic flux per resolution element as $F_i = B_{z,i}S$, where S is the area of a pixel, and $B_{z,i}$ is the longitudinal magnetic field strength of

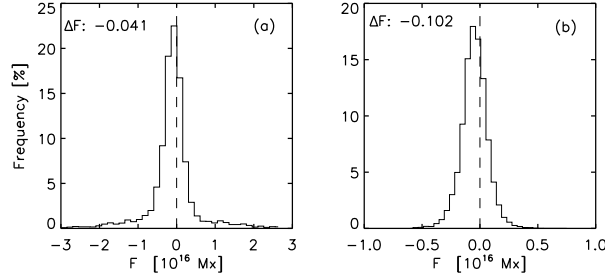


Figure 9. Histograms of magnetic flux per resolution element in the 300-MHD (a) and 140-MHD (b) regions. ΔF is the flux imbalance.

resolved i -element in our 2D simulation at the level $\log \tau_5 = 0$. Figure 9 presents the histograms for two simulated regions of the relative frequency of F_i within each bin. The maximum of these distributions is at about 1×10^{15} Mx. The signed magnetic flux density $\langle B_z \rangle$ in the 300-MHD and 140-MHD regions is -28 G and -40 G at $\log \tau_5 = 0$. The unsigned flux density $\langle |B_z| \rangle$ is 300 and 140 G, respectively. It is close to the values measured in actual observations of the magnetic network (Lites, 2002) and the ephemeral regions (Martin, 1988).

Following Lites (2002) we compute a flux imbalance as:

$$\Delta F = \frac{F^+ + F^-}{|F^+| + |F^-|},$$

where F^+ and F^- is positive and negative flux, defined as the sum of F_i fluxes directed towards and away from the observer, respectively.

The imbalance is an important characteristic of the magnetic flux distribution since it shows the degree of mixture of positive and negative fluxes. We find the imbalances in the 300-MHD and 140-MHD regions to be equal to -0.041 and -0.102 . According to Lites (2002), the flux imbalance for network regions varies from 0.02 to 0.95 depending on the observed region.

4.3. Line-of-sight Velocities

By analogy with the measurements of shifts of observed Stokes-V, we measure the Doppler shifts of the synthesized V profiles of the Fe I λ 1564.8 nm line relative to the rest wavelength. Positive (red) shifts correspond to downflows and negative (blue) shifts to upflows. Figure 10 (a, c) displays the histograms of the line-of-sight (LOS) velocities V_z derived from the zero-crossing shifts of the synthetic V profiles for two simulated regions at the surface of $\log \tau_5 = -1$. The mean velocity is equal to about 0.40 km s $^{-1}$ and -0.03 km s $^{-1}$ for 300-MHD and for 140-MHD regions, respectively. The width of the distribution ranges from -4 km s $^{-1}$ to 8 km s $^{-1}$ and from -4 km s $^{-1}$ to 4 km s $^{-1}$, respectively, for these regions. The larger the absolute magnetic flux density in the simulated region, the stronger the downflows in the magnetized plasma.

Figure 10 (e, g) shows the correlation between the velocity and the continuum intensity contrast $I_c / \langle I_c \rangle$ at λ 1564.8 nm. I_c is the continuum intensity

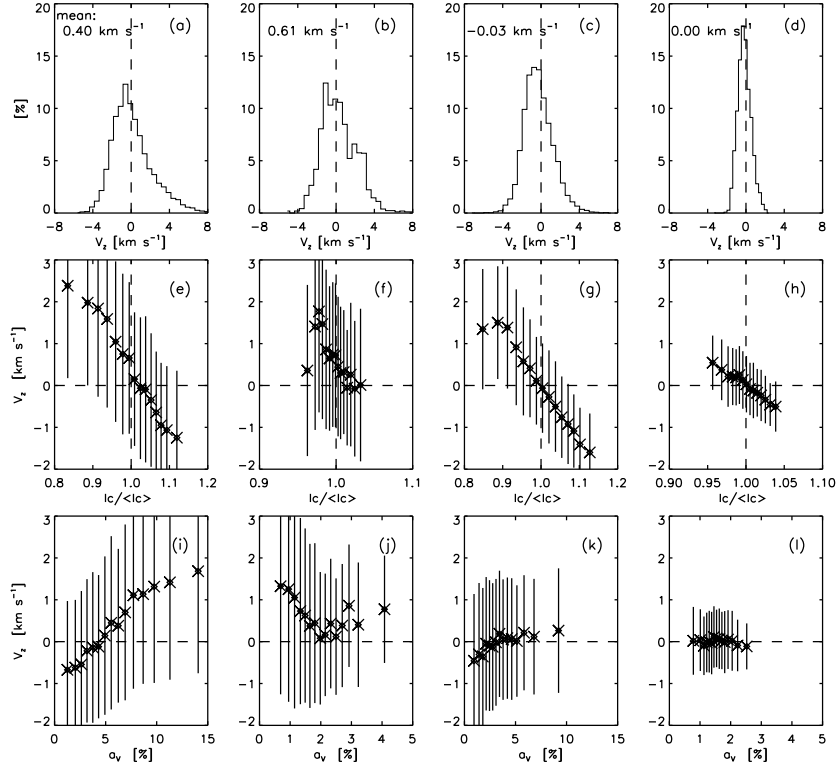


Figure 10. Histograms of vertical velocity V_z , and the statistical dependencies of V_z on the continuum intensity $I_c / \langle I_c \rangle$ and the amplitude a_V (indicator of magnetic flux density). The data are derived from synthetic Stokes-V profiles before (a, e, i) and after (b, f, j) their spatial smoothing in the 300-MHD region as well as before (c, g, k) and after (d, h, l) their spatial smoothing in the 140-MHD region. The V_z values are binned into a few intervals containing an equal number of points. Error bars indicate the standard deviation of the individual points within each interval.

in a pixel of a snapshot and $\langle I_c \rangle$ is the mean continuum intensity in the snapshot. Similar to observations, the regions of the simulated surface with the contrast more than 1 are called granules and the rest of regions around the granules are called intergranular lanes. As Figure 10 suggests, the upflow velocity within the granules of the 300-MHD (140-MHD) run is as large as about -1.2 (-1.8) km s⁻¹, on the average. We confirm the observed granular blueshift of the Stokes profiles. In the dark intergranular lanes, where fluxtubes are often located, an average downflow velocity is as large as about 2.5 (1.5) km s⁻¹. This is the intergranular redshift effect in the network regions. As to the observed intergranular redshifts, it should be noted that no significant systematic motions (± 0.25 km s⁻¹) inside fluxtubes are detected in spectropolarimetric observations with spatial resolution worse than $1''$ (e.g., Solanki, Stenflo, 1986). On the other hand, a predominance of downflows is found in observations with spatial resolution better than $1''$. In particular, Sigwarth *et al.* (1999) obtain a mean redshift of about 0.5 km s⁻¹ for magnetic structures of the network and the plages. Langangen *et al.* (2007) find downflows of about 0.2 – 0.7 km s⁻¹ at

the edges of magnetic elements (bright points, ribbons, and flowers). In addition, Langangen *et al.* (2007) also analyze realistic 3D magnetoconvective simulations and find downflows of 1.5–3.3 km s⁻¹, i.e., it is much stronger than observed. The reason is that there are strong horizontal gradients in the velocity field on the small scales at the periphery of fluxtubes. The observed redshifts are underestimated due to insufficient spatial resolution. Our simulated downflows of 1.5–2.5 km s⁻¹ agree well with the results of Langangen *et al.* (2007) and confirm the intergranular redshift effect in the network regions.

The dependence V_z on a_V in the 300-MHD region (Figure 10i) shows that the large V_z of the downflows, on the average 2 km s⁻¹, correspond to strong magnetic fields. The upflows, with V_z around 1 km s⁻¹, correspond to weak fields. Figure 10k illustrates the downflows in the 140-MHD region are smaller than in the 300-MHD region. In general, the statistical dependencies confirm the tight connection of the velocity field with small-scale magnetic fields in the solar photosphere.

Besides, Figure 10 (b, f, j as well as d, h, l, p) shows the velocity distribution and the statistical velocity dependencies obtained after spatial smoothing of Stokes-V profiles. The mean velocity is equal to 0.6 km s⁻¹ (300-MHD) and 0 km s⁻¹ (140-MHD). The larger the absolute flux density, the stronger the changes due to spatial smoothing. In particular, see the dependence of V_z on a_V .

Summarizing the results of our LOS velocity analysis it is necessary to point out that the mean LOS velocity is greater than zero within simulated strong network region with high value of unsigned flux density. This is a result dominated downflows which are appeared due to a formation of strong magnetic concentrations with $B_z > 1500$ G. The correlation between LOS velocities and the intensity contrast, and Stokes-V amplitudes is in agreement with the physical properties of convective motions in the photosphere. The variations of these parameters reflect the changes of the velocity field, temperature, and magnetic field of the solar plasma due to interaction of solar granules and small-scale magnetic fields in the observed photosphere. Granular flows and overshooting convection act to gather magnetic field lines and to redistribute magnetic flux on the solar surface. A fundamental property of the thermal convection in a stratified photosphere is the topological asymmetry between hot upflows and cool downflows. Until the magnetic field remains to be frozen in the plasma, i.e., until the field reaches the condition of equipartition, the magnetic flux is expelled from the granule interior to its boundaries, the intergranular lanes, and also the upper photospheric layers. The expulsion process may give rise to magnetic field strength up to 1000 G at the radiating layer level in the region of downflows (Gadun, 2000). Hence, downflows, strong magnetic field strength, and low temperature in the photosphere are related to each other. A similar statement is true for upflows, weak magnetic field strength, and high temperature.

4.4. Asymmetry of Stokes-V Profiles of the Fe I 1564.8 nm Line

The asymmetry of V profiles is an indicator of the dynamic processes in solar magnetized plasma. According to polarimetric observations (*e.g.*, Sánchez Almeida, Lites, 2000; Sigwarth, 2001; Socas-Navarro, Sánchez Almeida, 2002;

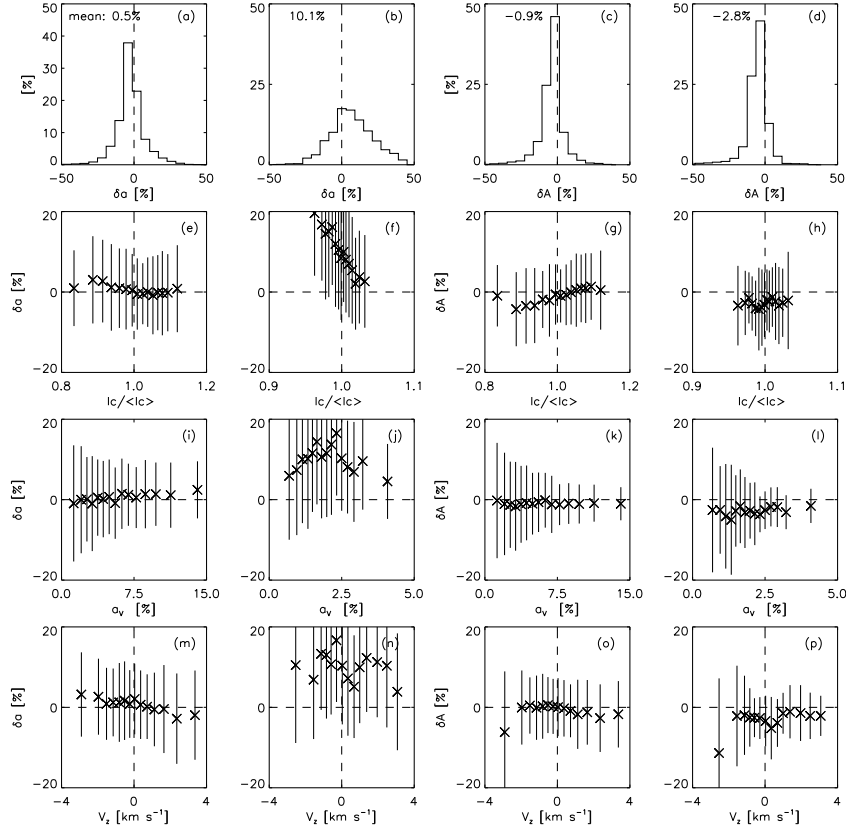


Figure 11. Histograms of amplitude δa and area δA asymmetries, and their dependencies on continuum intensity $I_c / \langle I_c \rangle$, amplitude a_V , and velocity V_z . These quantities are derived from synthetic Stokes-V profiles before (a, e, i, m as well as c, g, k, o) and after (b, f, j, n as well as d, h, l, p) their spatial smoothing in the 300-MHD region.

(Khomenko *et al.*, 2003), V profiles in active and quiet regions on the Sun are variable in shape. Almost all of them are asymmetric due to gradients of the magnetic and velocity fields along and across the line of sight (Solanki, 1993). Depending on the shape complexity, the profiles are said to be regular (two lobes of opposite signs) and irregular (three and more lobes or a single lobe).

We use the definition of the amplitude (δa) and area (δA) asymmetry of Solanki (1993). The amplitude and area asymmetry for the regular Stokes-V is defined as:

$$\delta a = \frac{|a_b| - |a_r|}{|a_b| + |a_r|}, \quad \delta A = \frac{|A_b| - |A_r|}{|A_b| + |A_r|},$$

where a_b , a_r , A_b , A_r are the amplitudes and areas of the blue and red wings.

The asymmetry of observed regular Stokes profiles has been studied by many authors (*e.g.*, Grossmann-Doerth, Keller, Schüssler, 1996, Martínez Pillet, Lites, Skumanich, 1997; Sigwarth *et al.*, 1999; Khomenko *et al.*, 2003). Previous and

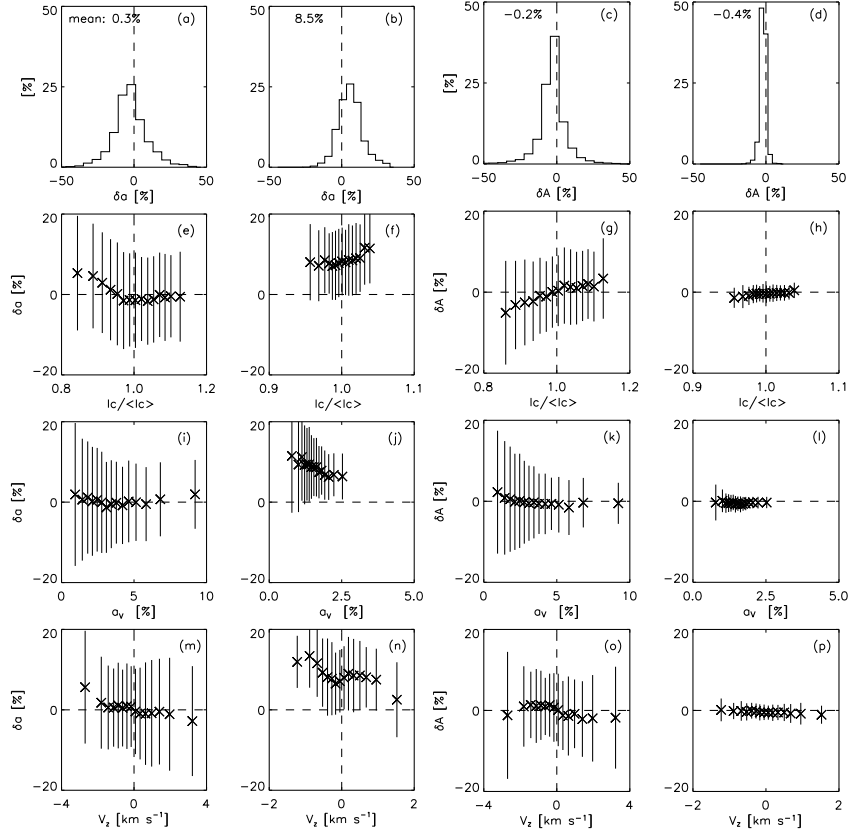


Figure 12. The same as Figure 11 but for the 140-MHD region.

new results show that outside sunspots at the disc center the majority of regular profiles have positive asymmetry of amplitudes and areas, i.e., the blue wing is stronger than the red one; the amplitude asymmetry is two times greater, on the average, than the asymmetry of areas. It was not clear for a long time why the amplitude asymmetry exceeds the area asymmetry.

Figures 11 and 12 (a, c) show the distribution of the amplitude and area asymmetries derived for the 300-MHD and 140-MHD regions. The mean asymmetry of synthetic V profiles in two simulated regions is very small: $\delta a = 0.5\%$ (0.3%) and $\delta A = -0.9\%$ (-0.2%).

It is interesting to note that the character of the statistical dependencies of δa and δA on the continuum intensity differ in the range $I_c / \langle I_c \rangle < 1$ (Figures 11e and 12g). It follows from the V profiles formed within intergranules which have mainly positive δa and negative δA . The magnitude of δa and δA for these V profiles is more than for the profiles formed in the granules. The other statistical dependencies (δa , δA on a_V and V_z) do not show a clear tendency.

Spatial smoothing drastically affects amplitude asymmetry of V-Stokes. The values of δa basically become positive and considerably larger for the majority of profiles. The dependence of δa on $I_c / \langle I_c \rangle$ also varies significantly. Large

δa mostly occurs in the profiles formed in intergranular lanes, where the effect of spatial smoothing is the greatest. On the average, $\delta a = 10.1\%$ (8.5%) and $\delta A = -2.8\%$ (-4%) in the V-Stokes synthesized with the 300-MHD (140-MHD) run. The spatial smoothing is one of the main reasons of the large observed amplitude asymmetry. δa is more sensitive to the atmospheric effects than δA . This may explain why the observed amplitude asymmetry is by a factor of two greater than the area asymmetry. Our results demonstrate that the asymmetry of synthetic profiles (without smoothing) is much smaller than that of smoothed ones. The asymmetry of irregular synthetic Stokes-V profiles is analyzed in detail by Sheminova (2005).

5. Conclusion

We use the realistic 2D MHD simulations of nonstationary magnetogranulation by Gadun, Sheminova, Solanki (1999a), with initial bipolar magnetic field, and with mean unsigned field strength of 54 G and 1.6 G. Two time sequences of snapshots with an absolute flux density of 300 G and 140 G are analyzed in detail. Most likely, the simulations reproduce magnetic structures similar to the strong and the weak network observed on the solar surface. Our results can be summarized as follows:

1. Based on the magnetic field strength probability density functions, PDFs, deduced from the two simulated regions, we find that the PDF shape depends on the initial conditions of the magnetic field, the absolute magnetic flux density in the given region, and height in the photosphere.

2. According to the magnetic field PDF obtained in the simulated strong network, the field strength varies from 1 G to 2800 G at $\log \tau_5 = 0$. The most probable field strength is about 250 G. The mean unsigned strength is about 500 G. The unsigned flux density is 300 G and the signed flux density is -28 G. The fields below 500 G fill most of the surface (70%) of given region. Very weak magnetic fields less than 100 G occupy 8% of the surface area, while the kG fields fill 9.7%. The filling factor of bright points with very strong kG fields ($B > 1500$ G) is equal to 4.2%.

3. The magnetic field strength in the simulated weak network varies from 1 G to 1100 G at the level $\log \tau_5 = 0$. The most probable field strength is 150 G. The mean unsigned magnetic field strength is about 250 G. The unsigned flux density is 140 G and the signed flux density is -40 G. The magnetic fields below 500 G occupy the major fraction (93%) of the surface. Very weak magnetic fields less than 100 G occupy 17% and the kG fields fill 0.3% of the surface.

4. The magnetic flux is below 0.5×10^{16} Mx in 90% of resolved elements of simulated regions. Varying magnetic polarities in the simulated regions produce a polarity imbalance of -0.10 and -0.04.

5. The average line-of-sight velocity depends on the unsigned flux density in the simulated region. The larger the magnetic flux density, the stronger the downflows in the region. On the average, the LOS velocities are 0.4 km s^{-1} in the simulated strong network and 0 km s^{-1} in the simulated weak network.

The velocity scatter is in the range from -4 km s^{-1} (upflow) to 8 km s^{-1} (downflow). On the average, the stronger downflows (about 2 km s^{-1}) occur in intergranular lanes filled by strong magnetic field, while the stronger upflows (about -1.5 km s^{-1}) occur in the granules. A close correlation are found between LOS velocity and the granular contrast as well as the magnetic field strength.

6. The amplitude and area asymmetries of synthetic Stokes-V profiles do not exceed 1%, on the average. If the V profiles are spatially smoothed to $1''$, the average amplitude asymmetry rises to 10% and the average area asymmetry is changed only slightly. Spatial averaging influences the amplitude asymmetry by a larger extent compared to the area asymmetry. This may be a reason why observed amplitude asymmetries are greater than area asymmetries.

Acknowledgements This study was carried out thanks to the great work of Aleksey Gadun who was the initiator of the investigations of simulated solar magnetogranulation and the main executor of the MHD simulation. Unfortunately, he will never be able to continue the work started by him so successfully. The author thanks to A. Gadun, S. Solanki, S. Ploner for the productive collaboration, E. Khomenko for a code for the spatial smoothing of Stokes profiles. The author is grateful to an anonymous referee for helpful comments and important suggestions to improve the presentation of the results and the content of the paper.

References

- Asplund, M., Ludwig, H.-G., Nordlund, Å., Stein, R.F.: 2000, *Astron. Astrophys.*, **359**, 669.
- Atroshchenko, I.N., Sheminova, V.A.: 1996a, *Kinematika i Fizika Nebes. Tel [Kinematics and Physics of Celestial Bodies]*, **12**, No. 4, 32.
- Atroshchenko, I.N., Sheminova, V.A.: 1996b, *Kinematika i Fizika Nebes. Tel [Kinematics and Physics of Celestial Bodies]*, **12**, No. 5, 32.
- Barklem, P.S., Piskunov, N., O'Mara, B.J.: 2000, *Astron. Astrophys. Suppl. series*, **142**, 467.
- Bellot Rubio, L.R., Collados M.: 2003, *Astron. Astrophys.*, **406**, 357.
- Bellot Rubio, L.R., Luis R., Rodrigues Hidalgo, I., Collados, M., Khomenko, L., Ruiz Cobo, B.: 2001, *Astron. Astrophys.*, **560**, 1010.
- Berger, T.E., Rouppe van der Voort, L.H.M., Löfdahl, M.G.: 2007, *Astron. Astrophys.*, **661**, 1272.
- Berger, T.E., Rouppe van der Voort, L.H.M., Löfdahl, M.G., Carlsson, M., Fossum, A., Hansteen, V.H., Marthinussen, E., Title, A., Scharmer, G.: 2004, *Astron. Astrophys.*, **428**, 613.
- Brandt, P.N., Gadun, A.S.: 1995, *Kinematika i Fizika Nebes. Tel [Kinematics and Physics of Celestial Bodies]*, **11**, no. 4, 44.
- Cameron, R., Galloway, D.: 2005, *Mon. Not. Roy. Astron. Soc.*, **358**, 1025.
- Carlsson, M., Stein, R.F., Nordlund, Å., Scharmer, G.B.: 2004, *Astrophys. J.*, **610**, L137.
- Cattaneo, F.: 1999, *Astrophys. J.*, **515**, L39.
- Collados, M.: 2001, in Sigwarth, M. (ed.), *Advanced Solar Polarimetry — Theory, Observation, and Instrumentation*, *ASP Conf. Ser.*, **236**, p. 255.
- de Wijn, A.G., Rutten, R.J., Tarbell, T.D.: 2005, *Astron. Astrophys.*, **441**, 1183.
- Delbouille, L., Roland, G., Neven, L.: 1973, *Photometric atlas of the solar spectrum from λ 3000 to λ 10000*, Liege, Institut d'Astrophysique.
- Deinzer, W., Hensler, G., Schüssler, M., Weisshaar, E.: 1984, *Astron. Astrophys.* **139**, 435.
- Domínguez Cerdeña, I., Sánchez Almeida, J., Kneer, F.: 2003, *Astrophys. J.*, **407**, 741.
- Domínguez Cerdeña, I., Sánchez Almeida, J., Kneer, F.: 2006a, *Astrophys. J.*, **636**, 496.
- Domínguez Cerdeña, I., Sánchez Almeida, J., Kneer, F.: 2006b, *Astrophys. J.*, **646**, 1421.

- Gadun, A.S.: 2000, *Kinematika i Fizika Nebes. Tel [Kinematics and Physics of Celestial Bodies]*, **16**, No. 2, 99.
- Gadun, A.S., Sheminova, V.A.: 1988, *SPANSAT: Program for LTE- calculation of Absorption Line Profiles in Stellar Atmospheres*, Inst. Theor. Phys. Kiev, preprint no. 88–87P, p. 37.
- Gadun, A.S., Sheminova, V.A., Solanki, S.K.: 1999a, *Kinematika i Fizika Nebes. Tel [Kinematics and Physics of Celestial Bodies]*, **15**, No. 5, 387.
- Gadun, A.S., Solanki, S.K., Johannesson, A.: 1999, *Astron. Astrophys.*, **350**, 1018.
- Gadun, A.S., Solanki, S.K., Sheminova, V.A., Ploner, S.R.O.: 2001, *Solar Phys.*, **203**, 1.
- Grossmann-Doerth, U., Keller, C.U., Schüssler, M.: 1996, *Astron. Astrophys.*, **315**, 610.
- Grossmann-Doerth, U., Larsson, B., Solanki, S.K.: 1988, *Astron. Astrophys.*, **204**, 266.
- Grossmann-Doerth, U., Schüssler, M., Steiner O.: 1998, *Astron. Astrophys.*, **337**, 928.
- Khomenko, E., Collados, M.: 2007, *Astrophys. J.*, **659**, 1726.
- Khomenko, E.V., Shelyag, S., Solanki, S.K., Vögler, A.: 2005a, *Astron. Astrophys.*, **442**, 1059.
- Khomenko, E.V., Collados, M., Solanki, S.K., Lagg, A., Trujillo Bueno, J.: 2003, *Astron. Astrophys.*, **408**, 1115.
- Khomenko, E.V., Martínez González, M.J., Collados, M., Vögler, A., Solanki, S.K., Ruiz Cobo, R., Beck, C.: 2005b, *Astron. Astrophys.*, **436**, L27.
- Langangen, Ø., Carlsson, M., Rouppe van der Voort, L., Stein, R.F.: 2007, *Astron. Astrophys.*, **655**, 615.
- Lin, H.: 1995, *Astrophys. J.*, **446**, 421.
- Lin, H., Rimmele T.: 1999, *Astrophys. J.*, **514**, 448.
- Lites, B.W.: 2002, *Astrophys. J.*, **573**, 431.
- Lites, B.W., Skumanich, A., Martínez Pillet, V.: 1998, *Astron. Astrophys.*, **333**, 1053.
- Lites, B.W., Kubo, M., Socas-Navarro, H., Berger, T., Frank, Z., Shine, R., Tarbell, T., Title, A., Ichimoto, K., Katsukawa, Y.: 2008, *Astrophys. J.*, **672**, 1237.
- Martin, S.F.: 1988, *Solar Phys.*, **117**, 243.
- Martínez González, M.J., Collados, M., Ruiz Cobo, B.: 2006, *Astron. Astrophys.*, **456**, 1159.
- Martínez Pillet, V., Lites, B.W., Skumanich, A.: 1997, *Astrophys. J.*, **474**, 810.
- Meunier, N., Solanki, S.K., Livingston, W.C.: 1998, *Astron. Astrophys.*, **331**, 771.
- Nagata, S., Tsuneta, S., Suematsu, Y., Ichimoto, K., Katsukawa, Y., Shimizu, T., Yokoyama, T., Tarbell, T.D., Lites, B.W., Shine, R.A.: 2008, *Astrophys. J.*, **677**, L145.
- Nordlund, Å.: 1985, in Schmidt H.U., (ed.), *Theoretical Problems in High Resolution Solar Physics*, München, p.101.
- Orozco Suárez, D., Bellot Rubio, L.R., Del Toro Iniesta, J.C., Tsuneta, S., Lites, B., Ichimoto, K., Katsukawa, Y., Nagata, S., Shimizu, T., Shine, R.A.: 2007, *Pub. Astron. Soc. Japan*, **59**, 837.
- Ploner, S.R.O., Solanki, S.K., Gadun, A.S.: 1999, *Astron. Astrophys.*, **352**, 679.
- Ploner, S.R.O., Schüssler, M., Solanki, S.K., Gadun, A.S.: 2001a, in Sigwarth, M. (ed.), *Advanced Solar Polarimetry — Theory, Observation, and Instrumentation*, ASP Conf. Ser., **236**, p. 363.
- Ploner, S.R.O., Schüssler, M., Solanki, S.K., Sheminova, V.A., Gadun, A.S., Frutiger, C.: 2001b, in Sigwarth, M. (ed.), *Advanced Solar Polarimetry — Theory, Observation, and Instrumentation*, ASP Conf. Ser., **236**, p. 371.
- Rouppe van der Voort, L.H.M., Hansteen, V.H., Carlsson, M., Fossum, A., Marthinussen, E., van Noort, M.J., Berger, T.E.: 2005, *Astron. Astrophys.*, **435**, 327.
- Sánchez Almeida, J.: 2004, in Sakurai, T., Sekii, T., (eds.), *The Solar-B Mission and the Forefront of Solar Physics*, ASP Conf. Ser., **325**, p. 115.
- Sánchez Almeida, J.: 2006, *Astron. Astrophys.*, **450**, 1199.
- Sánchez Almeida, J., Lites, B.W.: 2000, *Astrophys. J.*, **532**, 1215.
- Sánchez Almeida, J., Domínguez Cerdeña, I., Kneer, F.: 2003, *Astrophys. J.*, **597**, L177.
- Sánchez Almeida, J., M'arquez, I.M., Bonet, J.A., Domínguez Cerdeña, I., Muller, R.: 2004, *Astrophys. J.*, **609**, L91.
- Schüssler, M.: 2003, in Trujillo Bueno, J., Sánchez Almeida J., (eds.), *Solar Polarization 3*, ASP Conf. Ser., **307**, p. 601.
- Shelyag, S., Schüssler, M., Solanki, S.K., Vögler, A.: 2007, *Astron. Astrophys.*, **469**, 731.
- Sheminova, V.A.: 1999, *Kinematika i Fizika Nebes. Tel [Kinematics and Physics of Celestial Bodies]*, **15**, No. 5, 398.
- Sheminova, V.A.: 2003, *Kinematika i Fizika Nebes. Tel [Kinematics and Physics of Celestial Bodies]*, **19**, No. 2, 107.
- Sheminova, V.A.: 2004, *Kinematika i Fizika Nebes. Tel [Kinematics and Physics of Celestial Bodies]*, **20**, No. 3, 1.

-
- Sheminova, V.A.: 2005, *Kinematika i Fizika Nebes. Tel [Kinematics and Physics of Celestial Bodies]*, **21**, No. 3, 172.
- Sheminova, V.A., Gadun, A.S.: 2000, *Astron. Rep.*, **44**, 701.
- Sigwarth, M.: 2001, *Astrophys. J.*, **563**, 1031.
- Sigwarth, M., Balasubramaniam, K.S., Knölker, M., Schmidt, W.: 1999, *Astron. Astrophys.*, **349**, 941.
- Socas-Navarro, H., Sánchez Almeida, J.: 2002, *Astrophys. J.*, **565**, 1323.
- Socas-Navarro, H., Sánchez Almeida, J.: 2003, *Astrophys. J.*, **593**, 581.
- Solanki, S.K.: 1993, *Space Sci. Rev.*, **63**, p.188.
- Solanki, S.K., Stenflo, J.O.: 1986, *Astron. Astrophys.*, **170**, 120.
- Solanki, S.K., Rüedi, I.K., Livingston, W.: 1992, *Astron. Astrophys.*, **263**, 312.
- Stein, R.F., Nordlund, Å.: 2000, *Solar Phys.*, **192**, 91.
- Stein, R.F., Nordlund, Å.: 2002, in Sawaya-Lacoste, H., (ed.), *SOLMAG 2002. Proceedings of the Magnetic Coupling of the Solar Atmosphere Euroconference and IAU Colloquium*, **188**, ESA Publications Division, p. 83.
- Stein, R.F., Nordlund, Å.: 2006, *Astrophys. J.*, **642**, 1246.
- Stein, R.F., Bercik, D., Nordlund, Å.: 2002, *Il Nuovo Cimento*, **25C**, no. 5-6, 513.
- Steiner, O.: 1996, in Schmitt D., Voigt H. (eds.), *Solar and Galactic Magnetic Fields*. Göttingen, Vandenhoeck and Rupprecht, p. 15
- Steiner, O.: 2003a, *Astron. Astrophys.*, **406**, 1083.
- Steiner, O.: 2003b, in Erdelyi R., Petrovay K., Roberts, B., Aschwanden M. (eds.), *Turbulence, Waves, and Instabilities in th Solar Plazma*. NATO Advanced Research Workshop, Kluwer, p. 117
- Steiner, O.: 2007, in Kneer F., Puschmann K.G., Wittmann A.D. (eds), *Modern Solar Facilities - Advanced Solar Science*, Proceedings of a Workshop, Universitätsverlag Göttingen, p. 321.
- Steiner, O., Rezaei, R., Schaffenberger, W., Wedemeyer-Böhm, S.: 2008, *Astrophys. J.*, **680**, L85.
- Vögler, A., Shelyag, S., Schüssler, M., Cattaneo, F., Emonet, T., Linde, T.: 2005, *Astron. Astrophys.*, **429**, 335.
- Weiss, N.O., Proctor, M.R.E., Brownjohn, D.P.: 2002, *Mon. Not. Roy. Astron. Soc.*, **337**, 292.